

Non-convex, ringing-free, FFT-accelerated solver using an incremental approximate energy functional

Ali Falsafi^{a,*}, Richard J. Leute^b, Martin Ladecký^c, Till Junge^a

^a*Department of Mechanical Engineering, École Polytechnique Fédérale de Lausanne, 1015 Lausanne, Switzerland*

^b*Department of Microsystems Engineering, University of Freiburg, Georges-Köhler-Allee 103, 79110 Freiburg, Germany*

^c*Faculty of Civil Engineering, Czech Technical University in Prague, Thákurova 7, 166 29 Prague 6, Czech Republic*

Abstract

Fourier-accelerated micromechanical homogenization has been developed and applied to a variety of problems, despite being prone to ringing artifacts. In addition, the majority of Fourier-accelerated solvers applied to fast Fourier transform (FFT)-accelerated schemes only apply to convex problems. We here introduce a first order approximation incremental energy functional (FAIEF) that allows to employ modern efficient and non-convex iterative solvers, such as trust-region solvers or Low memory Broydon-Fletcher-Goldfarb-Shanno (LBFGS) in a FFT-accelerated scheme. These solvers need the explicit energy functional of the system in their standard form. We develop a modified trust region solver, capable of handling non-convex micromechanical homogenization problems such as continuum damage employing the FAIEF. We use the developed solver as the solver of a ringing-free FFT-accelerated solution scheme, namely the projection based scheme with finite element discretization.

Keywords: computational homogenization, FFT-based solvers, Non-convexity, Trust region solvers, Alkali-Silica reaction

1. Introduction

Mechanical homogenization, motivated by the idea of representing a heterogeneous micro-structure as an equivalent homogeneous medium, aims to calculate effective mechanical properties of micro-structures, including homogenized elastic constants and the stress-strain response given the micro-structure and constitutive laws of the individual components. For simple micro-structures (e.g. micro-structures containing only linear elastic phases) the effective properties of a heterogeneous material can be estimated analytically [2, 49, 56, 24, 47, 46, 54].

*Corresponding author

Email address: `ali.falsafi@epfl.ch` (Ali Falsafi)

However, when the micro-structure of a material gets more complex, analytical methods are generally no longer suitable for the determination of the effective properties.

Computational homogenization, on the other hand, is an effective method in up-scaling the behavior of complex micro-structures specially those consisting of, i. highly nonlinear, or ii. evolving phases [23, 17]. Computational homogenization methods are based on the construction of a micro-scale boundary value problem, the so-called cell problem, discretizing the solution domain and solving the governing equation, equilibrium equation for instance, using numerical schemes such as finite element method (FEM) [71] or spectral methods [52, 12].

One of the primary applications of computational homogenization is in multi-scale simulations, where it enables resolving the full micro-structure and studying the influence of parameters at microscale on the solution of a structural problem [71, 37, 70, 42]. In a multiscale scheme, such as FEM squared (FE^2), discretization points (quadrature points) at the macro-scale are each represented by a representative volume element (RVE) in which the micro structure of the underlying phases is captured. The strains at macro-scale discretization points are imposed as boundary conditions on the micro-scale model and the resultant mean stress and effective tangent extracted from the solution of the cell problem is passed to the macro-scale. In a multi-scale approach, usually, the computational costs of the cell problem solution outweighs that of the higher scale problem since in a single macroscale load step the RVE solver is called at least once per material point. Accordingly, it is of high importance to optimize and speed-up the RVE solution. In comparison with FEM, the computational efficiency of the cell problem solution can be significantly improved using fast Fourier transform (FFT)-based methods [31, 64, 62].

As fast and reliable RVE solvers, FFT-based methods have gained much attention in the last 20 years [76, 81, 69]. FFT-based methods exploit the simple structure of regular grids and allow one to use lightweight iterative solvers such as Newton-conjugate gradient (CG) for solving computational homogenization problems [80, 48]. By contrast, in the conventional FEM framework, due to poor scaling of linear solution complexity (caused by deterioration of spectral characteristics of the corresponding linearized system with growing the size of the problem), iterative solvers are not a good choice unless being equipped with preconditioners and direct solvers are the used most of the time [50]. FFT-based methods are, therefore, roughly 200 times faster compared to the conventional FEM scheme [12] solving problems with roughly 10^4 degree of freedom (DoF)s and higher. FFT-based methods are also less memory consuming (due to their inherent matrix-free formulation [69]) compared to FEM. In addition, solution domain discretization is trivial since the RVE is only implicitly meshed.

Increasing the resolution and improving solution accuracy is straightforward in spectral methods. As a result, large-scale micro-structures simulations are more efficient using spectral methods compared to conventional FEM. The computational complexity of FFT-based solution in the Fourier-Galerkin (FG) scheme [10] is dominated by the FFT algorithm ($\mathcal{O}(n \log n)$, where n is the number of the discretization points in the RVE solution domain). The avail-

ability of highly optimized FFT implementations (*FFTW* [15] and *PFFT* [59]) makes efficient implementation of spectral methods simple.

Spectral methods, in addition to their original scheme (iterative solution of an integral equation of the Lippmann-Schwinger type) as introduced by Moulinec et al. [52, 60] can be derived by applying the Galerkin method using trigonometric polynomials as shape functions (FG method) [76, 81]. The global support and the oscillatory nature of trigonometric functions results in Gibbs ringing phenomenon [40] which makes them unsuitable for problems containing localized phenomena such as continuum damage and non-linear plasticity. Gibbs ringing artifact occurs near abrupt transitions as spurious fluctuations in the solution of the problem (strain and stress field in case of mechanical computational homogenization) due to discrete Fourier transformation truncation. Gibbs-ringing is well-known and well-documented, for instance in [21, 22, 18, 20, 40]. Sharp discontinuity with high phase contrast exacerbates Gibbs-ringing, thus, Gibbs ringing is more pronounced in problems containing phases with high contrast, for instance RVEs containing highly contrasted composites [45] or void in the micro-structure such as foams [41].

Several approaches have been used to address Gibbs-ringing in spectral methods, e.g. [78, 70, 30, 39]. These methods can be categorized into two main categories i. mitigation: these approaches try to reduce the Gibbs-ringing artifact fluctuations by smoothing the geometry of the phase interfaces [29] or by using higher order discrete derivatives [70], or ii. elimination: removing the Gibbs-ringing by using discrete derivatives obtained from a regular periodic FEM discretization [35, 34]. The projection based method in [35] is capable of eliminating the Gibbs ringing while maintaining all the advantages of the FFT-based methods mentioned earlier. A preconditioned displacement based FEM scheme mathematically equivalent to the projection-based scheme of Leute et al. [35] has been developed recently by Ladecký et al. [33]. In their FFT-accelerated finite element (FE) scheme, a preconditioner derived based on the Green's function of a uniform periodic reference medium is used to make the distribution of system matrix eigenvalues favorable for iterative solvers [32, 63]. Such discretized Green's functions are mathematical convolutions and therefore their inversion and application is cost-effective in the Fourier space.

Use of Newton-CG due to its quadratic convergence properties is common in FFT-based solution schemes [19, 28, 75, 81]. However, it is notable that Newton-CG is unable to handle problems with non-convex energy functional (symmetric non-positive semi definite (SNPSD) system matrix) such as homogenization of RVEs containing meta-materials [36] or continuum damage [1, 41]. Conventional non-linear FEM solvers are also susceptible to instabilities in modeling non-convex problems [58].

A possible solution, called sequential linear algorithm (SLA) [65, 67, 68, 11, 66], for circumventing the solution of non-convex problems is breaking the non-linear non-convex problem to a sequence of linear convex problems. In SLA, in each solution step, only one integration point is allowed to soften by certain reduction of its stiffness due to damage [57]. SLA is an event-driven algorithm and therefore it does not scale with problem size since by increasing problem

size damage sites (possible event sites) increases rapidly; therefore, SLA becomes inefficient. This is a major drawback for solving a cell problem in a multi-scale model [6].

Non-convex iterative solvers, for instance nonlinear CG, quasi-Newton solvers such as Low memory Broydon-Fletcher-Goldfarb-Shanno (LBFGS) [55, 8], and also trust region solvers [79, 55] are typically developed for optimization of problems with known objective functions. However, in mechanical engineering problems, the objective function (strain energy functional) is often not known or difficult to calculate for complicated constitutive laws. In context of FFT-accelerated solvers [77] has used quasi-Newton solvers for convex problems using an inexact line search method, but the application to non-convex problems still remains not investigated.

In this paper, we introduce a first order approximation incremental energy functional (FAIEF) that enables application of non-convex solvers for problems whose objective function explicit form is not available. The introduced FAIEF is a first order approximation and is only valid for small load steps. However, this is typically not an issue because many homogenization problems, such as nonlinear computational homogenization problems, already meet this condition as for solving them the load increments are chosen to be small.

We opted for trust-region Newton-CG solver to illustrate the applicability of the introduced FAIEF for solving non-convex problems whose energy functional evaluation is not easy. In addition, we demonstrate how the projection-based scheme with FE discretization [35], in conjunction with the introduced trust region solver [55] (equipped with the introduced FAIEF), can successfully and efficiently solve homogenization damage problems with a SNPSD Hessian matrix.

The projection-based scheme with FE discretization as well as the employed non-convex solvers are explained in Section 2. In Section 3, we show that the modified trust region Newton-CG, developed and introduced in this paper, yields identical results compared to the standard trust region Newton-CG solver in a simplistic 1D example. The convergence properties of the modified trust-region solver are resolution independent, as we show by presenting the modified trust region Newton-CG solver performance for variation of RVE sizes. In addition, we show that the modified trust region solver can solve a real-world damage homogenization problem that suffers both from SNPSD stiffness and sharp phase interface with unbounded contrast. We have implemented all methods in the open source code μ Spectre [27] and all numerical examples in Section 3 can be reproduced by executing the corresponding scripts provided in the supplementary material.

2. Methods

In the following, we consider a rectangular periodic RVE; see Figure 1 for illustration of a typical micro-structure. Small strain micro-mechanical formulation is adopted for the derivations of the equilibrium of a micro-structure undergoing a displacement field of $\chi : \Omega_0 \rightarrow \Omega$ which maps the grid points from

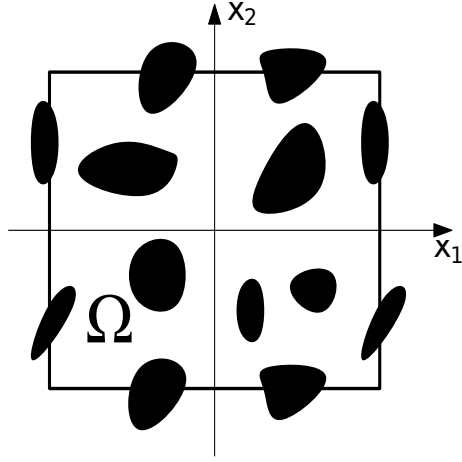


Figure 1: Rectangular two-dimensional cell with outlined periodic micro-structure obtained from Ref. [33].

undeformed positions Ω_0 to their deformed configurations Ω . The material response corresponding to position \mathbf{x} , given the local strain $\boldsymbol{\varepsilon}(\mathbf{x})$ is determined by constitutive law of the material at that point as $\boldsymbol{\sigma}(\mathbf{x}, \boldsymbol{\varepsilon}(\mathbf{x}))$. The total strain $\boldsymbol{\varepsilon}$ can be decomposed to average strain tensor \mathbf{E} and the periodic fluctuating strain field $\tilde{\boldsymbol{\varepsilon}}(\mathbf{x})$:

$$\boldsymbol{\varepsilon}(\mathbf{x}) = \mathbf{E} + \tilde{\boldsymbol{\varepsilon}}(\mathbf{x}) \quad \forall \mathbf{x} \in \Omega_0, \quad \text{s.t.} \quad \int_{\Omega_0} \tilde{\boldsymbol{\varepsilon}}(\mathbf{x}) d\mathbf{x} = \mathbf{0} \quad (1)$$

The governing mechanical equilibrium equation in this domain reads as:

$$-\nabla_0 \cdot \boldsymbol{\sigma}(\mathbf{E} + \tilde{\boldsymbol{\varepsilon}}(\mathbf{x}), \mathbf{x}) = 0, \quad \forall \mathbf{x} \in \Omega_0. \quad (2a)$$

$$\tilde{\boldsymbol{\varepsilon}} = \nabla_{0,s} \tilde{\mathbf{u}} \in \mathcal{E} \quad \tilde{\mathbf{u}} : \Omega_0 \text{ periodic displacement} \quad (2b)$$

where ∇_0 is the *nabla* operator (∇_0 is gradient operator and $\nabla_0 \cdot$ is the divergence operator) in the reference coordinates and $\nabla_{0,s}$ stands for the symmetrized *nabla* operator ($\nabla_{0,s} = \frac{1}{2}(\nabla_0 + \nabla_0^T)$) in the reference coordinates. The compatibility equation (2b) dictates the strain field to be a gradient field.

In the projection-based spectral scheme, in order to solve the equilibrium equation, the local equilibrium equation in its weak form after applying Gauss divergence theorem casts to:

$$\int_{\Omega_0} \check{\boldsymbol{\zeta}}(\mathbf{x}) : \boldsymbol{\sigma}(\mathbf{E} + \tilde{\boldsymbol{\varepsilon}}(\mathbf{x}), \mathbf{x}) d\mathbf{x} = 0 \quad \forall \check{\boldsymbol{\zeta}} \in \mathcal{E}. \quad (3)$$

Note that the boundary term cancels out due to periodic boundary condition. The strain is taken to be from the compatible gradient space \mathcal{E} .

The test function in the projection-based spectral methods ($\check{\zeta}$ in (3)) is in strain space while in the FEM formulation, the test function is a displacement field. Therefore, the test function of projection-based spectral methods is not an arbitrary field (unlike FEM). Proceeding with the Galerkin discretization necessitates having a fully arbitrary test function. Therefore, in order to apply the Galerkin discretization on (3), it is necessary to impose compatibility condition on the test variable $\zeta(\mathbf{x})$. Zeman et al. [81] have introduced a compatibility projection operator \mathbb{G} based on the Fourier discretization to impose compatibility. The operator \mathbb{G} maps any second-order tensor to its compatible (periodic gradient) contribution. Applying the projection operator on the test variable $\zeta(\mathbf{x})$ makes it possible to continue with the Galerkin discretization and solve directly for strain field.

In the following of this section, after elaborating the projection operator \mathbb{G} and the resulting discretized equilibrium equation, the remedy of the ringing artifact developed by Leute et. al [35] is reviewed. Next, its extension to trust region solver capable of handling generic homogenization problems with non-convex energy functions such as damage mechanics problems is explained.

2.1. Projection based solver

The key element of projection-based spectral solvers is the projection operator \mathbb{G} which enforces compatibility on an arbitrary field $\zeta(\mathbf{x})$ as:

$$\begin{aligned}\check{\zeta}(\mathbf{x}) &= [\mathbb{G} \star \zeta](\mathbf{x}) \\ &= \int_{\Omega_0} \mathbb{G}(\mathbf{x} - \mathbf{y}) : \zeta(\mathbf{y}) \, d\mathbf{y} \quad \forall \mathbf{x} \in \Omega_0.\end{aligned}\quad (4)$$

Applying projection yields compatible contribution $\check{\zeta}(\mathbf{x})$ of the original field $\zeta(\mathbf{x})$. In (4), \star is the convolution operator. The convolution format of (4) makes its application in Fourier space convenient, since convolution in real space is equivalent to contraction in Fourier space. Accordingly, (4) can be rewritten as:

$$\check{\zeta}(\mathbf{x}) = \mathcal{F}^{-1}\{\widehat{\mathbb{G}}(\mathbf{k}) : \widehat{\zeta}(\mathbf{k})\} \quad (5)$$

where $\widehat{\mathbb{G}}(\mathbf{k})$ is the compatibility operator in Fourier basis, $\widehat{\zeta}(\mathbf{k}) = \mathcal{F}\{\zeta(\mathbf{x})\}$, and \mathbf{k} is the discrete frequency vector in the Fourier domain. Considering that $\widehat{\mathbb{G}}$ is a fourth order block diagonal tensor, the equilibrium equation (3) combined with the compatibility equation (5) yields [81]:

$$\widehat{\mathbb{G}}(\mathbf{k}) : \widehat{\boldsymbol{\sigma}}(\mathbf{k}) = \mathbf{0}. \quad (6)$$

Using Newton's method to solve the nonlinear system of (6) iteratively, the $(i+1)^{th}$ update of the strain field $\boldsymbol{\varepsilon}_{i+1}$ in the iterative scheme can be calculated from the previous approximation of the strain field $\boldsymbol{\varepsilon}_i$ incremented by a finite strain increment $\delta\boldsymbol{\varepsilon}_{i+1}$,

$$\boldsymbol{\varepsilon}_{i+1} = \boldsymbol{\varepsilon}_i + \delta\boldsymbol{\varepsilon}_{i+1}. \quad (7)$$

Starting from an initial strain approximation $\boldsymbol{\varepsilon}_0$ the strain increment at each step is given by solution of the linear system:

$$\widehat{\mathbb{G}} : \mathbb{B}_i : \delta \boldsymbol{\varepsilon}_{i+1} = - \widehat{\mathbb{G}} : \boldsymbol{\sigma}_i \quad (8)$$

at the $(i + 1)^{th}$ nonlinear solution step, where \mathbb{B}_i is the constitutive tangent matrix of the system evaluated at discretization points.

Leute et al. [35] derived a general expression for the operator $\widehat{\mathbb{G}}$ as an explicit function of the second rank tensor $\widehat{\mathbf{g}}$ with the form of:

$$\widehat{\mathbf{g}}(\mathbf{k}) = \frac{\widehat{\mathcal{D}}(\mathbf{k}) \otimes \widehat{\mathcal{D}}^*(\mathbf{k})}{\widehat{\mathcal{D}}(\mathbf{k}) \cdot \widehat{\mathcal{D}}^*(\mathbf{k})}, \quad (9)$$

where $\widehat{\mathcal{D}}$ is the derivative operator in Fourier space, and $*$ denotes the Hermitian transpose. The form of the projection operator $\widehat{\mathbb{G}}$ as a function of $\widehat{\mathbf{g}}$ is different in small strain and finite strain formulation (further details can be found in [81, 35]).

In the original projection based method developed by Zeman et al. [81], $\widehat{\mathcal{D}}$ was expressed based on the Fourier basis as $\widehat{\mathcal{D}}(\mathbf{k}) = i\mathbf{k}$ which yields a second rank tensor $\widehat{\mathbf{g}}$ of the form:

$$\widehat{\mathbf{g}}_{\alpha\beta}(\mathbf{k}) = \begin{cases} \mathbf{0} & \text{if } \mathbf{k} = \mathbf{0}, \\ \frac{\mathbf{k}_\alpha \mathbf{k}_\beta}{k^2} & \forall \mathbf{k} \neq \mathbf{0}, \end{cases} \quad (10)$$

in index notation, where \mathbf{k} s are normalized discrete Fourier wave-vectors. Leute et al. [35] showed that, based on the general form of the projection operator ($\widehat{\mathbb{G}} = \widehat{\mathbb{G}}(\widehat{\mathbf{g}})$ explicitly formulated in [10] in both finite-strain and small strain formulation), it is possible to derive projection operators using gradient operator obtained from different discretization schemes of choice. For instance, Leute et al. [35] worked out a projection operator based on a linear FE discretization and showed that using the basis functions of a FE discretization results in elimination of Gibbs ringing artifacts. This makes use of FE discretization suitable for problems with highly localized phenomena such as damage mechanics. In the following of this paper, the derivations are carried out for a spectral method with FE basis set.

Choosing different $\widehat{\mathcal{D}}$ in a projection based spectral method is equivalent to choosing different element types and shape functions in the conventional FEM formulation. The operator $\widehat{\mathcal{D}}$, for a FE discretization, is calculated using the derivative of the corresponding shape functions. Similar to a FE scheme, the strain, stress, and the constitutive tangent are evaluated at the quadrature point of the FE discretization.

Optimal spectral characteristics of the system matrix in (8) [63] makes linear iterative solvers and specifically CG solver ideal for solving it. However, solving (8) with CG solver needs Hessian matrix \mathbb{B}_i to be symmetric positive semi definite (SPSD) which is not the case in several mechanical homogenization problems such as meta-materials [36] or continuum damage [1, 41]. In the subsection 2.2, a trust region Newton-CG solver is adopted to expand the use of the projection-based spectral method to non-convex problems.

2.2. Non-convex optimization

The projection-based spectral scheme explained in Subsection 2.1 due to the optimal spectral characteristics of its linearized system [63] enables us to benefit from the computational advantages of iterative solvers such as Newton-CG. This results in great scaling for solving RVEs with large number of discretization points. As set forth above, CG can only solve linear system of equations with SPSD matrix.

Therefore, in order to be able to benefit from the computational speed-up offered by the projection based spectral scheme for problems with SNPSD system matrices, we need to employ other iterative solvers. Possible candidates capable of handling non-convex problems are nonlinear CG, quasi-Newton solvers, and Trust region Newton solver. In this paper, a trust region Newton solver as a robust and memory efficient solver capable of handling non-convexity in an iterative fashion is adopted to be used in homogenization problems.

The potential of trust region solvers (as well as quasi-Newton solvers) has not been exploited in computational homogenization, since in a considerable part of the literature, conventional FEM employing direct solvers used to be the de-facto for computational homogenization. As a result, the main challenge of using trust region and quasi Newton solvers in computational homogenization, namely missing an explicit expression of the objective function in the equivalent energy minimization counterpart of the equilibrium solution, has not been addressed to the authors' best knowledge. This problem is addressed in the following of this section after a review over the standard trust region Newton solver.

2.2.1. Trust region Newton solver

In contrast to conventional line search algorithms, in a trust region solver, the approximate model (sub-problem) "trusted" within a bounded region (trust region) near the current iterate is minimized iteratively until a minimizer of the original function is reached [55, 3, 4]. In the trust region solution strategy, optimization is carried out by minimizing a model function (typically quadratic) trusted up to a certain radius of the current iterate as a proxy problem (sub-problem). The approximate model is derived from the local information gathered from the objective function at the current iterate.

There is no a-priori knowledge of the radius of the region in which the model can adequately approximate the objective function. In addition, the model's accuracy declines by moving away from the current iteration. Therefore, it is crucial to determine the "trust region" of the model function and to regulate it consistently during the solution process.

To this end, based on the model's match with the original objective function, the trust region is adjusted in each iteration. As a general rule, the trust region can be expanded if the approximate model fits the original problem well. In contrast, the trust region shrinks if the approximate model fails to estimate the original function adequately [26]. It is therefore necessary to access the original objective function of the equivalent optimization problem if one needs to use a trust region solver in its standard formulation.

Let us consider the total energy function, equivalent to the original objective function of a homogenization problem, of the RVE as:

$$W = \sum_Q w(\boldsymbol{\varepsilon}^Q, \mathbf{g}(\mathbf{x}^Q)) \quad (11)$$

where w denotes energy at Q s, which are the discretization quadrature points, and $\mathbf{g}(\mathbf{x})$ represents the internal variables of the material.

The solution of the equilibrium equation (2a) is, in particular, corresponding to the critical point of the total energy function (11). In the projection-based scheme the equilibrium problem is solved in strain state space. According to the fact that the energy conjugate of strain is stress, the gradient of the energy with respect to strain is actually the stress tensor. In addition, the Hessian of the objective function corresponds to the tangent stiffness of the material at the discretization points,

$$\nabla_{\boldsymbol{\varepsilon}} W = \boldsymbol{\sigma}, \quad (12)$$

$$\nabla_{\boldsymbol{\varepsilon}}^2 W = \mathbb{B}. \quad (13)$$

One possible sub-problem model (and probably the most common form) of the trust region solver is a quadratic energy function approximation in form of:

$$m_i(\mathbf{p}_i) = W(\boldsymbol{\varepsilon}_i) + \nabla_{\boldsymbol{\varepsilon}} W^T \mathbf{p}_i + \frac{1}{2} \mathbf{p}_i^T \mathbb{B}_i \mathbf{p}_i, \quad s.t. \|\mathbf{p}_i\| < R_i, \quad (14)$$

where in the Newton trust region solver, \mathbb{B}_i is taken as the Hessian matrix of the energy evaluated (\mathbb{B}) at quadrature points at i^{th} load step and R_i is the radius of the trust region. \mathbf{p}_i is a solution step in the strain space. Here, the energy functional is taken as a direct function of strains at i^{th} solution step as in the projection based formulation the equations are solved in strain space. Other trust region solvers are also possible using different choices for the matrix \mathbb{B}_i .

The agreement of the actual objective function ($W(\boldsymbol{\varepsilon}_i + \mathbf{p}_i)$) and the model ($m_i(\mathbf{p}_i)$) at the new iterate is evaluated by a scalar variable at the i^{th} iterative step, defined as:

$$\rho_i = \frac{W(\boldsymbol{\varepsilon}_i) - W(\boldsymbol{\varepsilon}_i + \mathbf{p}_i)}{m_i(\mathbf{0}) - m_i(\mathbf{p}_i)}. \quad (15)$$

In the trust region algorithm, the value of ρ_i , as set forth in [55], determines how the trust region size will be updated as well as whether or not the proposed step will be accepted.

It is relatively simple to calculate the denominator of the right hand side of the (15) ($\Delta m_i = m_i(\mathbf{0}) - m_i(\mathbf{p}_i)$) according to the definition of $m_i(\mathbf{p}_i)$ given in (14). For calculation of the nominator, explicit expression of the origin objective function (equivalent to stored energy in mechanical engineering problems) is necessary. In mechanical homogenization problems, however, the objective function is often not calculable (at least easily), since the actual energy density function of most materials is very complex (and even impossible to compute). A first order incremental energy function that allows us to use trust region solvers

to solve generic non-convex mechanical homogenization problems is presented here. In order to derive the incremental energy functional, first, Taylor series of the actual energy function W is expanded at both $\boldsymbol{\varepsilon}_i$ and $\boldsymbol{\varepsilon}_i + \boldsymbol{p}_i$ points as:

$$W(\boldsymbol{\varepsilon}_i + \boldsymbol{p}_i) = W(\boldsymbol{\varepsilon}_i) + (\nabla_{\boldsymbol{\varepsilon}} W|_{\boldsymbol{\varepsilon}_i})^T \boldsymbol{p}_i + \frac{1}{2} \boldsymbol{p}_i^T (\nabla_{\boldsymbol{\varepsilon}}^2 W|_{\boldsymbol{\varepsilon}_i}) \boldsymbol{p}_i + \mathcal{O}(\|\boldsymbol{p}_i\|^3), \quad (16a)$$

$$\begin{aligned} W(\boldsymbol{\varepsilon}_i) &= W((\boldsymbol{\varepsilon}_i + \boldsymbol{p}_i) - \boldsymbol{p}_i) \\ &= W(\boldsymbol{\varepsilon}_i + \boldsymbol{p}_i) - (\nabla_{\boldsymbol{\varepsilon}} W|_{\boldsymbol{\varepsilon}_i + \boldsymbol{p}_i})^T \boldsymbol{p}_i + \frac{1}{2} \boldsymbol{p}_i^T (\nabla_{\boldsymbol{\varepsilon}}^2 W|_{\boldsymbol{\varepsilon}_i + \boldsymbol{p}_i}) \boldsymbol{p}_i + \mathcal{O}(\|\boldsymbol{p}_i\|^3). \end{aligned} \quad (16b)$$

Subtracting (16a) from (16b) and dropping higher order terms yields:

$$\begin{aligned} W(\boldsymbol{\varepsilon}_i + \boldsymbol{p}_i) - W(\boldsymbol{\varepsilon}_i) &\approx \\ &\frac{1}{2} \left((\nabla_{\boldsymbol{\varepsilon}} W|_{\boldsymbol{\varepsilon}_i})^T \boldsymbol{p}_i + (\nabla_{\boldsymbol{\varepsilon}} W|_{\boldsymbol{\varepsilon}_i + \boldsymbol{p}_i})^T \boldsymbol{p}_i \right) + \\ &\frac{1}{4} \left(\boldsymbol{p}_i^T (\nabla_{\boldsymbol{\varepsilon}}^2 W|_{\boldsymbol{\varepsilon}_i}) \boldsymbol{p}_i - \boldsymbol{p}_i^T (\nabla_{\boldsymbol{\varepsilon}}^2 W|_{\boldsymbol{\varepsilon}_i + \boldsymbol{p}_i}) \boldsymbol{p}_i \right) \end{aligned} \quad (17)$$

Truncating (17) up to first order gives:

$$W(\boldsymbol{\varepsilon}_i + \boldsymbol{p}_i) - W(\boldsymbol{\varepsilon}_i) \approx \overline{\Delta W} = \frac{\boldsymbol{\sigma}(\boldsymbol{\varepsilon}_i + \boldsymbol{p}_i) + \boldsymbol{\sigma}(\boldsymbol{\varepsilon}_i)}{2} : \boldsymbol{p}_i. \quad (18)$$

The terms in the right hand side of (18) consist of the stress tensors at the previous and current trial steps which are already evaluated at all of the quadrature points. To take $\overline{\Delta W}$ as a valid estimation of ΔW , it is necessary to keep the load increments small. Furthermore, it is vital that the variation of resulting displacement field remains bounded. For instance, problems such as buckling under prescribed growing force does not satisfy boundedness of displacement field around the critical load; and therefore does not converge using the modified trust-region solver presented here. On the other hand, problems such as mechanics damage modeling are solvable using the modified solver presented here given that the applied load increments are controlled to be small.

The actual system energy reduction in the nominator of (15) can be replaced by the first order incremental energy approximation $\overline{\Delta W}$ calculated by energy (17) which gives an estimation of ρ ; denoted by $\bar{\rho}$ according to:

$$\bar{\rho}_i = \frac{\overline{\Delta W}}{\Delta m_i}. \quad (19)$$

It is notable that the evaluation of $\bar{\rho}_i$ needs the stress of the previous solution step to be stored.

Introducing the first order approximation of the energy functional enables us to use the robust trust region algorithm in cases that the explicit expression of W function is missing. The pseudo-algorithm of the projection-based trust-region solver is presented in Algorithm 2 which shows how the scalar value

ρ (or its estimated counterpart $\bar{\rho}_i$) is used to make decisions of accepting or rejecting trial step ($\delta\mathbf{F}$) as well as shrinking or expanding the trust region. As shown in Algorithm 2, the memory overhead of using Trust region Newton-CG is storing the flux (stress) field at the previous solution step which does not impact the overall required for the solution compared to Newton-CG.

The predicted reduction of the model (m_i) will always be non-negative since the step \mathbf{p}_i is calculated by minimizing the model m_i over the region that includes $\mathbf{p} = \mathbf{0}$. Therefore, if $\bar{\rho}_i$ is negative, the value of the objective function at the new iterate ($W(\boldsymbol{\varepsilon}_i + \mathbf{p}_i)$) is greater than the current objective value ($W(\boldsymbol{\varepsilon}_i)$), thus the step must be rejected. Alternatively, if $\bar{\rho}_i$ is close to 1, it is safe to expand the trust region for the next step since the model m_i and the original objective function W are in good agreement over the solution step \mathbf{p}_i . In the case when $\bar{\rho}_i$ is positive but smaller than one, the trust region is not altered, however in the case when $\bar{\rho}_i$ is close to zero or negative, the trust region is shrunk by reducing R_i at the next iteration. How these decisions are made is depicted in details in Algorithm 2.

The solution of the subproblem (minimizing m within the ball of radius R) is easy to find when \mathbb{B} is positive definite and the minimizer is located within the trust region (equivalent to finding an unconstrained minimizer of the quadratic function m). There is no such simple solution to the subproblem in other cases. For these cases the minimizer resides on the boundary of the trust region. The constrained linear solver used here as the sub-problem solver is based on the solver introduced by Steihaug [55, 73] which is used to generate the trial solution step \mathbf{p}_i .

In addition, in order to make the linear solver robust to numerical rounding error problems a reset algorithm based on the work of Powell [61], and Dai et al. [9] was added to the linear solver algorithm. The used reset mechanism replaces the conjugate gradient step with a restart step (for instance, the gradient descent step) whenever two successive solution steps inside the linear solver (\mathbf{r}_j and \mathbf{r}_{j-1}) are not sufficiently orthogonal to each other. The measure expressing the orthogonality of the solution steps can be calculated by:

$$r_{\triangleleft} = \frac{|\mathbf{r}_j \cdot \mathbf{r}_{j-1}|}{\|\mathbf{r}_j\|^2}. \quad (20)$$

Comparing the measure r_{\triangleleft} by a constant value in the range of (0.1, 0.9) has been proposed as the decision criteria for restarting CG. We chose 0.2 as suggested in [61], hence the restart procedure is invoked if the measure r_{\triangleleft} is greater than 0.2.

Several quasi-Newton solvers also depend on the explicit expression of the objective function (e.g. LBFGS). Using the approximated strain energy reduction $\overline{\Delta W}$ instead of ΔW makes use of these quasi-Newton solvers possible as well. As derived here, the introduced incremental approximation of the objective function, specifically, enables us to use trust region Newton-CG solver following the algorithm given in Algorithm 2 (as the Newton nonlinear solver) and the algorithm given in Algorithm 1 as the subproblem solver. The introduced

approximate energy functional can be generalized to solve any other problem in which the explicit objective function is not available or not easy to calculate while the gradient and Hessian of the objective function are available.

3. Results and discussion

In the following, three examples are presented to demonstrate the solver developed above are presented. We first compare the performance of the modified trust region solver with that of the Newton-CG solver and the standard trust region solver on a very simple example. This example deals with a 1D damage spring system where the potential energy functional of the system is known. The trust-region solver can therefore be used on this system. Second, we test the correctness of the solution of the solver considering a convex system. The Eshelby inhomogeneity, whose analytical solution is available, is selected, so we can compare the generated solution of the modified trust region solver with the analytical solution of the problem. Finally, the capability of the solver for solving non-convex problems is demonstrated in a real world damage mechanics problem. As illustrated in this example the modified trust region solver can handle damage mechanics homogenization problems with rather complex constitutive laws.

3.1. Minimal 1D non-convex example

As a simple mechanical system with non-convex energy functional, a periodic 1D spring system (schematic shown in Figure 2a) consisting of three nodes connected with springs (k_0 , k_1 , and k_2) is taken as the first example. The springs k_1 and k_2 are elastic springs with $k_1 = k_2 = k$, while k_0 is a bi-linear damage spring, i.e. after a certain deformation threshold γ_0 its mechanical behavior switches from elastic to strain-softening. The force-displacement response of the k_0 spring is depicted in Figure 2b, The tangent of the strain-softening phase of the constitutive behavior is αk . Therefore, the post-peak stiffness matrix of the system becomes:

$$\mathbf{K} = \begin{bmatrix} (1 + \alpha)k & -k & -\alpha k \\ -k & 2k & -k \\ -\alpha k & -k & (1 + \alpha)k \end{bmatrix} \quad (21)$$

whose eigenvalues are $[\lambda_1 = 0, \lambda_2 = 3k, \lambda_3 = (2\alpha + 1)k]$. The third eigenvalue can be either positive or negative and for values $\alpha < -(1/2)$, the system is not positive semi definite (PSD) anymore, since it has one negative eigenvalue.

The problem has been solved with $k = 1.0$, $\gamma_0 = 0.1$ and for different values of α . The boundary condition of mean stretch equal to $\bar{x} = 0.11$, large enough to invoke post peak behavior of the k_0 spring, is imposed. Three different solvers listed in Table 1 are employed to solve the equilibrium of the 1D spring system. The functions needed to be explicitly evaluated in these solvers' algorithms are noted in Table 1.

Table 1: Solvers used to solve 1D spring example

Solver		Functions needed as input		
		Objective (Energy)	Gradient (Force)	Hessian (Stiffness)
i	Newton-CG SciPy	✗	✓	✓
ii	Trust Region Newton-CG Scipy	✓	✓	✓
iii	Modified Trust Region Newton-CG	✗	✓	✓

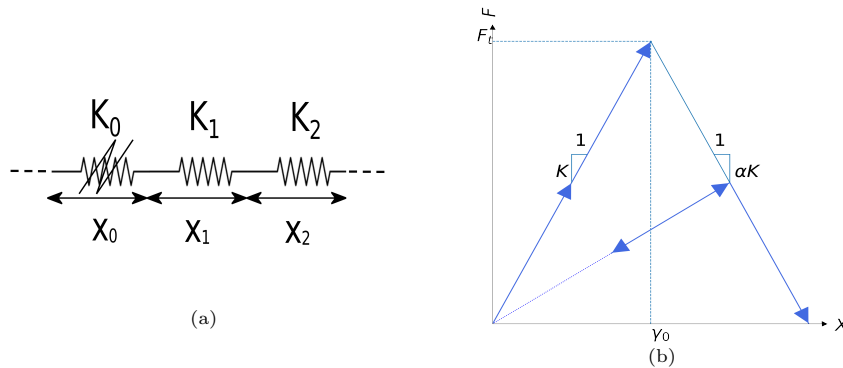


Figure 2: Periodic 1D spring example schematic and constitutive behavior of the damage spring 0^{th} spring, a. Schematic of 1-D damage spring example, b. Force-displacement response of the damage spring

The main difference between the modified and the standard trust region solver, as also noted in Table 1, is that explicit evaluation of the objective function is not needed in the modified solver.

The strain energy functional of the system as a function of the independent variable x_0 for the imposed boundary condition of $\bar{x} = 0.11$ is represented in Figure 3 for three different values of α , respectively from left to right, corresponding to convex, meta-stable, and concave energy surfaces. The variation of energy, and the final solution of the solvers listed in Table 1 are depicted in this figure. It is clear that in non-convex cases, Newton-CG solver is not capable of finding the energy functional minimum, while both standard and modified trust-region Newton-CG solvers converged to minimizer of the energy (equilibrium points). The hyper-parameters of the standard and the modified trust region solvers (such as initial and maximum trust-region radius) are chosen to be identical, this causes the solution steps of the solvers to coincide solving the 1D spring system.

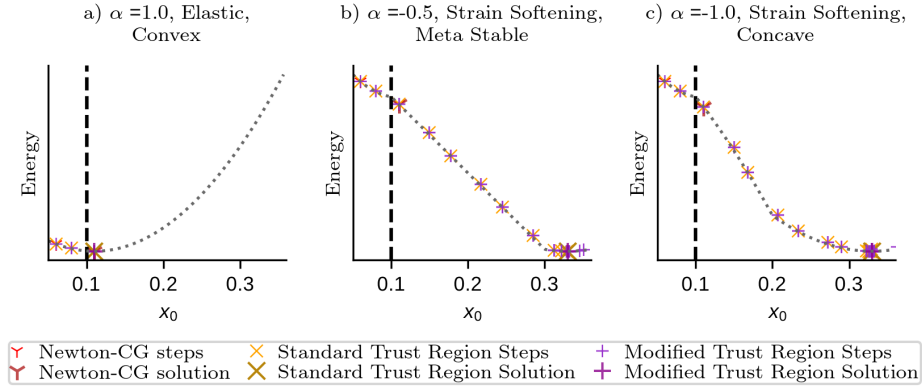


Figure 3: The energy of 1D spring system, schematically depicted in Figure 2a, over the solution trajectory of different solvers as a function of x_0 , for (a) Convex $\alpha = 1$ (b) Meta-stable $\alpha = -1/2$, (c) non-convex $\alpha = -1$ problems. In non-convex cases ((b), (c)), there is a concave point located at $x_0 = 0.1$ as the strain-softening behavior of the k_0 springs is activated from that point on. Dashed line is the energy functional of the system as a function of x_0

The transition of the energy functional from convexity to non-convexity is depicted in Figure 3 for $\alpha < -0.5$. In Figure 3a, the energy functional is convex over all values of x_0 while in Figure 3b and Figure 3c, the energy functional around the transition point ($x_0 = 0.1$) of the spring k_0 is non-convex.

This simple example can clearly show the equivalence of the obtained results with that of the standard trust region algorithm. The availability of the energy functional of this example makes the standard trust-region solver applicable. However, in general non-convex homogenization problems, the energy functional is not always available and therefore the standard trust-region solver is not an option and one can use the modified version with the approximated energy functional.

3.2. Convex example

In order to examine the introduced modified trust-region solver solving convex problems, a small-strain Eshelby inhomogeneity elasticity problem is chosen here as the second numerical example. The Eshelby inhomogeneity is an ellipsoidal body embedded in an infinite elastic medium, where the material properties of the inhomogeneity differ from those of the matrix. The analytical solution of the problem is known [13, 14, 53, 44]. A 2D example identical to the Eshelby inhomogeneity example presented by Leute et al. [35] is considered here as our second example. The linear FE discretization of Leute et al. [35] is adopted and the problem is solved by two solvers, namely the plain Newton-CG solver and our modified trust region Newton-CG solver.

The schematic of the RVE geometry is presented in column (a) of Figure 4. Figure 4 illustrates the solution of both Newton-CG and modified trust-

region Newton-CG (column (b)). Column (c) consists the difference of the solution of these two solvers. Figure 4 depicts that the solution of the two solvers are identical with respect to the solution tolerance (η_{NR} in Algorithm 2) taken for the iterative solution termination and the slight difference is in order of magnitude of the tolerance.

The number of Krylov solver and nonlinear solution steps needed to solve for equilibrium versus trust radius variation (maximum trust region radius) is plotted in Figure 5 which shows that in a convex problem the number of nonlinear solution steps as well as the accumulative number of the Krylov solver steps needed to reach the solution decays to that of Newton-CG solver as the size of the trust region increases for all grid point counts.

Figure 5 also shows that, in order to maintain the same number of nonlinear solution steps for solving a problem with twice as many grid points in each direction (4 times discretization points), the trust region should be roughly doubled. This correlation is rooted in the fact that the trust region radius is actually the radius of the hyper-sphere in the space of problem unknowns (strain in case of projection-based solver). Imagine the discretization of a problem is refined by a factor of N in each spatial direction in a 2D problem. This results in N^2 scaling of the number of the discretization points. Accordingly, the size of an equivalent solution step scales by N , in other words, an equivalent step in the problem with refined discretization is N times larger. As a result, to maintain the ratio of the solution step length constant with respect to trust region radius, The trust region radius should be scaled by a factor of N . This finding suggests that in order to use the trust region solver effectively one should loosen the trust region for larger problem sizes. However, it should be noted that the trust region radius is actively corrected during the solution of non-convex problems according to the accuracy of the sub-problem model functional.

3.3. Non-convex damage example

As the third example, we will discuss an interesting real-world example, namely alkali-silica reaction (ASR) damage homogenization. ASR is one of the most widespread causes of internal concrete deterioration [25, 74]. It is of great importance due to its economical significance since it concerns critical structures such as dams [72]. ASR is initiated by a chemical reaction between the alkali content of the cement paste and the silica in the aggregates. Humidity is critical for initiation of this chemical reaction as it washes the alkali content of the cement paste into the aggregate phase. The resultant of this process (known as ASR gel) as a result of its hydrophilic nature absorbs a considerable amount of water and therefore expands. Due to their expansion, the confined ASR gel pockets subject their surrounding to highly localized stresses. The induced stress can damage the concrete micro-structure by creating microcracks which will grow as the ASR advances. Following coalescing of the cracks, advancement of ASR damage can result in macroscopic cracks and stiffness and strength loss.

This example deals with RVE scale ASR damage modeling, in which we solve equilibrium equation of a problem with a non-convex energy functional, where

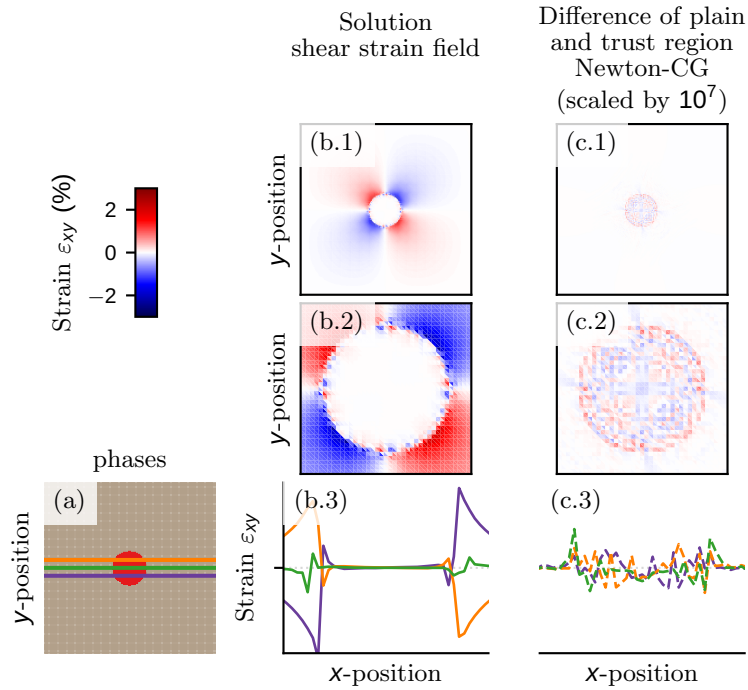


Figure 4: Solution of the cylindrical Eshelby inhomogeneity problem under mean spherical strain of 0.01 ($\epsilon_{xx} = \epsilon_{yy} = 0.01, \epsilon_{xy} = 0$). Column a. shows the phase distribution of a soft inhomogeneity cylindrical Eshelby inhomogeneity problem (showing the inhomogeneity in red). Column b. shows solution of cylindrical Eshelby inhomogeneity with Newton-CG and Trust region Newton-CG as they look the same. The column (c) consists the difference of Newton-CG and Trust region Newton-CG solutions scaled by a factor of 10^7 to make the difference visible. The first row shows the variation of the shear strain all over the solution domain. Second row shows the same variable zoomed around the inhomogeneity. The third row shows the variation of shear strain over the green, purple and orange cuts (located at the center-line, $r/2$ below and above of the center-line of the inhomogeneity) in subfigure a. The third row also corresponds to the zoomed area around the inhomogeneity.

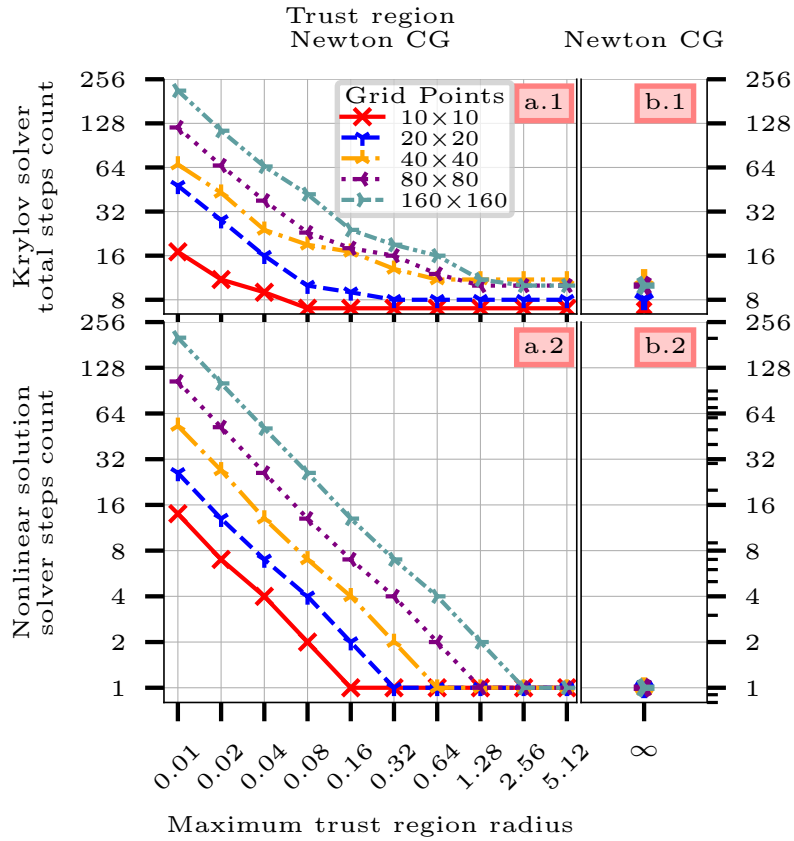


Figure 5: Number of Krylov steps (the first row) and number of nonlinear solution steps (the second row) needed for solving the Eshelby inhomogeneity problems for different number of grid points for the Newton-CG (column (a)) and as a function of initial trust region radius of trust region Newton-CG (column (b)). Number of nonlinear steps includes Newton steps and failed trial or trust region steps during the equilibrium solution

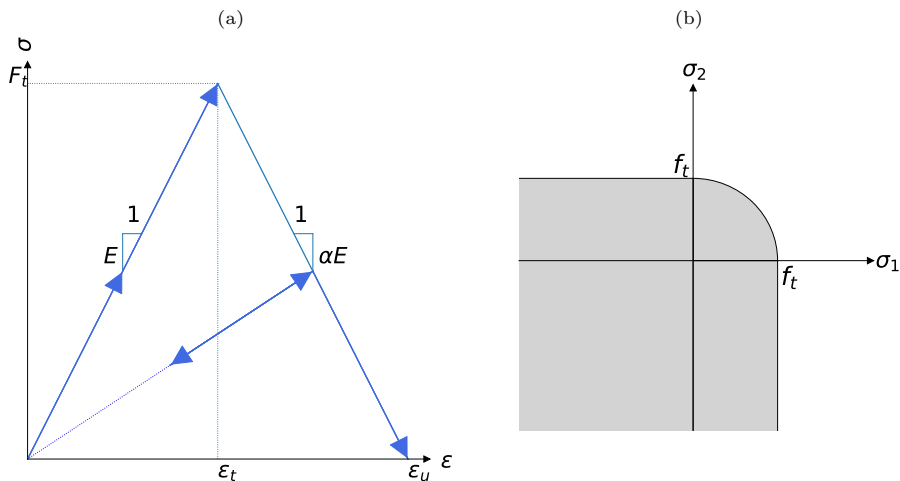


Figure 6: Constitutive law of the damage material in ASR damage example, a. stress-strain response of the damage material and b. Failure criterion of the damage material

the explicit expression of the functional is missing. The extremely high computational costs of this problem, namely ASR damage simulation has made it really challenging to conduct a comprehensive multi-scale modeling of ASR [7, 6]. In this example, we will present how the modified trust region solver developed in this paper applied in the projection-based scheme with FE discretization can offer a robust non-convex RVE solver which suites ASR damage simulation and with its quasi-linear scaling can make efficient multi-scale ASR simulation possible.

In order to be able to compare our results with available ASR damage meso-scale simulation results [6], a 2D meso-scale ASR damage model RVEs is considered here. We also report the RVE stiffness reduction, as an important measure for expressing the extent of ASR damage development [6]. In order to have same boundary conditions to [6] we imposed mean stress value as the boundary condition of the RVE. In order to impose mean stress value, we applied the necessary changes on the projection operator \mathbb{G} according to [38].

In 2D RVEs of this example, cement paste and aggregates are explicitly resolved as two different phases. Aggregates are placed inside a cement paste matrix in RVEs according to Fuller size distribution [51]. Pixels considered to be containing growing ASR gel pockets has been randomly inserted inside aggregates. The structure of the 2D micro-structure is depicted in Figure 7a.

The constitutive laws of both aggregate and cement paste phases are a bilinear crack band damage with an isotropic damage measure [43]. The initial Young modulus of E^0 and its damaged counterpart (E) can be related through:

$$E = (1 - D)E^0, \quad (22)$$

where the damage variable D can vary between 0 for intact material to 1 for

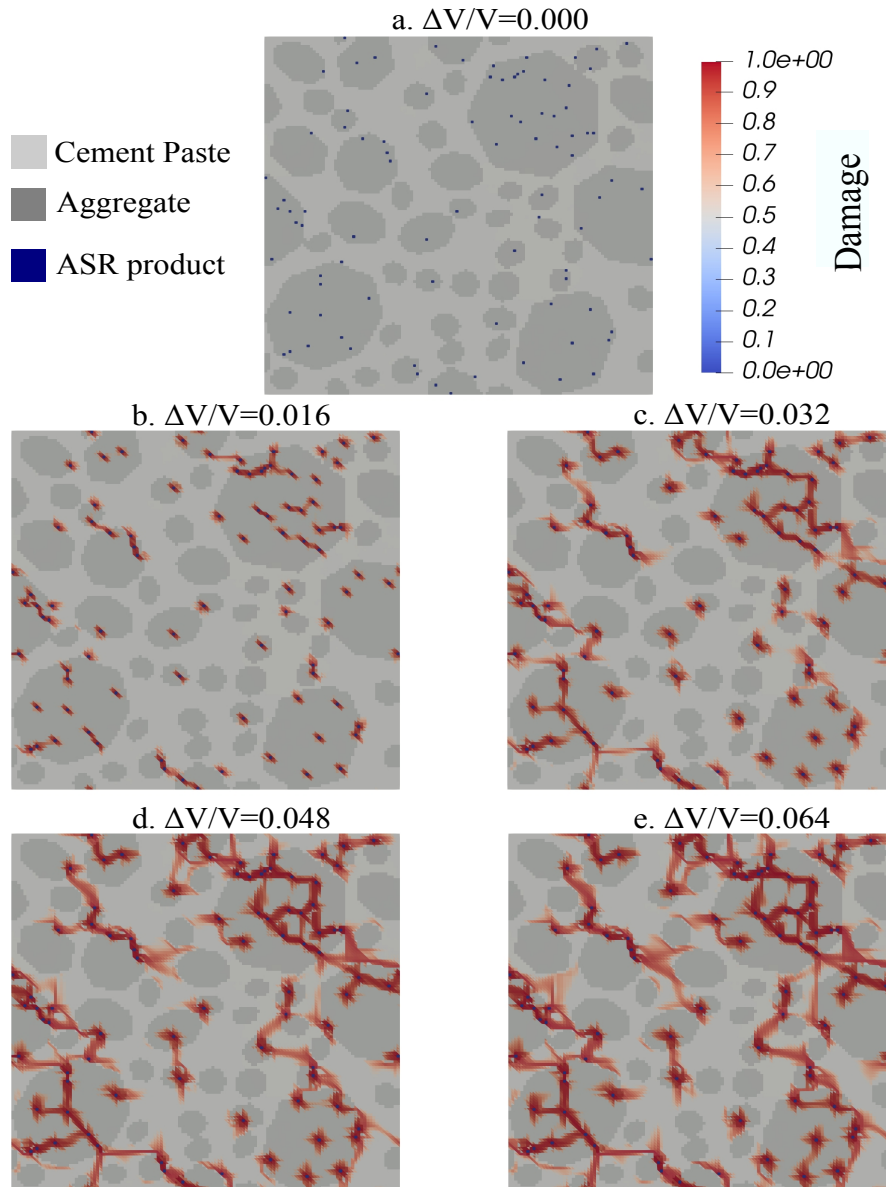


Figure 7: Evolution of crack pattern in the concrete micro-structure as a result of application of eigen-strain at ASR product sites shown as dark blue dots in the subfigure a. subfigures from a to e are arranged in a chronological sense and show snapshots of crack evolution inside the micro-structure as a function of increasing eigen-strain.

Table 2: Material properties of the non-convex damage example obtained from Ref. [16] for characteristic size $l_c = 5 \times 10^{-4}m$

	E [GPa]	μ [GPa]	ν	G_c [J/m ²]	f_t^0 [MPa]
Aggregates	59	22.6	0.3	160	10
Cement paste	12	4.6	0.3	60	3
ASR product	11	4.7	0.18	-	-

completely damaged (fractured) material. Further details of the damage constitutive law is presented in Appendix A. This constitutive behavior is also depicted schematically in Figure 6 where the subfigures (a) and (b) respectively illustrate the stress-strain response and the failure criteria of the constitutive law. As illustrated in Figure 6b, the damage material only fails under tensile loads.

The parameters of the constitutive law, listed in Table 2 are obtained from Ref. [16]. The damage part of this constitutive law leads to a SNPSD system matrix. For different discretization sizes, we conduct energy-based constitutive law regularization to preserve the Mode-I fracture energy (G_c) of the damage constitutive law and make the solution of the equilibrium independent of the mesh size.

We model the expansion of the ASR product sites by applying eigenstrain on the pixels containing them. Growing eigenstrain is added to the strain associated to these quadrature points before their constitutive law evaluation. These specific pixels are modeled as a linear elastic phase and assumed to contain the growing ASR gel pockets inside them. Line 28 of the Algorithm 2 is where eigenstrain is actually applied on the system. The mean value of stress is imposed as a boundary condition to be zero (free expansion) for the RVE. Imposing mean stress value as the boundary condition is implemented by means of modifying the projection operator following [38]. This choice of boundary condition allows us to compare the results to similar results in the literature.

Crack pattern advancement inside a sample RVE of physical size of $0.1m \times 0.1m$ is depicted in Figure 7. As shown in Figure 7b, the damage initiation sites are adjacent to the growing gel pixel sites in the RVE. The advancement of the cracks caused by ASR damage is depicted in Figure 7c-e. These subfigures illustrate the crack coalescence process as the ASR expansion proceeds. Crack coalescence depends on the distance between the gel pocket and the aggregate boundary as well as the distance to other gel pockets. Crack coalescence occurs earlier at crack sites near the boundary of the aggregates or other gel pockets.

Next, we conducted the discretization study and the load step study on a RVE with free expansion and growing gel pixels. In order to be able to realize nominally equivalent load scenarios by variation of the discretization size we have kept the area expansion of the pixels containing ASR gel pockets constant.

The effective stiffness reduction for a micro-structure subjected to similar area expansion of gel pocket pixels is presented with different discretization

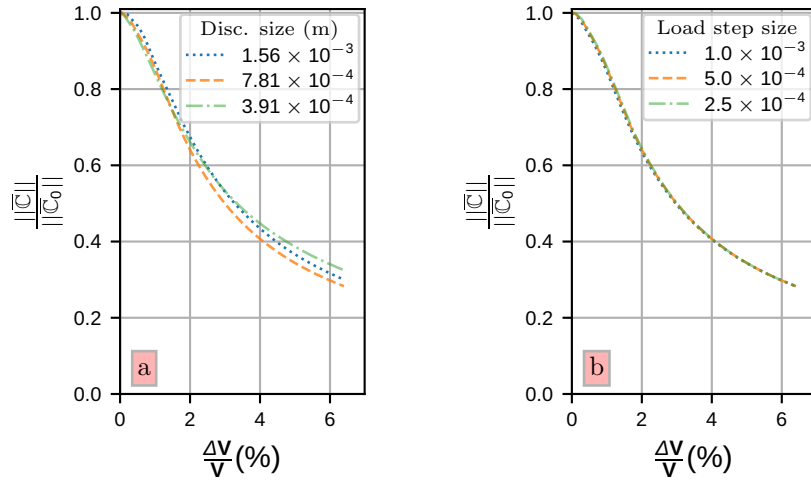


Figure 8: Discretization (mesh size) and load step study of the stiffness deterioration of 2D ASR damage simulation expressed as the ratio of the norm of the effective stiffness $\|\bar{C}\|$ tensor during ASR advancement divided by the norm of the effective stiffness tensor of the intact RVE $\|\bar{C}_0\|$. in subfigure a) the stiffness reduction of the same problem with fine ($h_f = 3.91 \times 10^{-4} m$), medium ($h_m = 2h_f$), and coarse ($h_c = 4h_f$) grid carried out with the medium load step size ($\Delta\varepsilon_m^{\text{eig}} = 5.0 \times 10^{-4}$) is plotted. In subfigure b) the stiffness reduction of the same problem with Load step study with small ($\Delta\varepsilon_s^{\text{eig}} = 2.50 \times 10^{-4}$), medium ($\Delta\varepsilon_m^{\text{eig}} = 2\Delta\varepsilon_s^{\text{eig}}$) and large load step of ($\Delta\varepsilon_l^{\text{eig}} = 4\Delta\varepsilon_s^{\text{eig}}$) carried out on h_m . is plotted.

in Figure 8a and load step size in Figure 8b. Figure 8a shows that the results obtained are independent of discretization size as the result of fine, medium and coarse grain are matching. The stiffness reduction of the medium grid size with different load step size application illustrates that the results are also independent of load step size.

According to the results of the discretization study we have chosen the medium grid size and a load step size of 5.00×10^{-4} (the medium value of the considered load steps) to conduct the simulations with different randomly generated micro-structures in the following of the paper whose results are depicted in Figure 9. We then subjected 100 randomly generated concrete 2D micro-structures to ASR expansion (imposed as eigenstrain in pixels containing gel pockets) under free expansion boundary condition. The shaded blue area in Figure 9a shows the distribution of the stiffness loss of these micro-structure vs imposed volumetric expansion of the gel pixels. The mean of the distribution is also plotted as solid blue line. The stiffness loss of 3 representative micro-structures are plotted in Figure 9a and the Figure 9b-d are their corresponding final crack pattern.

In addition, the results obtained by Cuba Ramos [6] modeling ASR damage in a similar configuration though using FEM scheme and using a different approach for addressing the numerical instabilities due to the non-convexity of the problem (namely SLA) is also plotted in Figure 9a labeled as Ref which depicts reasonable agreement with our obtained results. By using our modified trust region solver in the projection-based scheme with FE discretization our solution is much faster than their approach. According to correspondence with the authors of [6, 16] their calculations on 28 cores take roughly 48 hours while our simulations, on average, take half an hour on 16 cores on the same machine (Fidis cluster at Ecole Polytechnique Fédérale de Lausanne (EPFL)) which shows significant improvement on a 2D ASR damage simulation. The small differences visible in Figure 9 is probably due to subtle distinctions between the models, namely we have used rectangular elements containing ASR gel pockets while they were triangular in their model. The aggregates in their model are assumed to have circular geometry while they were ellipsoidal in our model. The differences in the application of the boundary conditions can also be source of difference between the models as they have traction free boundary conditions while we have applied zero mean stress on our RVE. However, despite of all this subtle differences our obtained stiffness loss is in a good agreement with their results.

4. Summary and conclusion

In this paper, we present a first order incremental approximation of the strain energy functional, which makes it possible to use fast ringing-free spectral solvers for non-convex problems, such as damage mechanics. We have derived the approximated energy functional based on the Taylor expansion of the energy functional of the system. Using the introduced incremental energy functional enables employing modern optimization techniques such as quasi-Newton

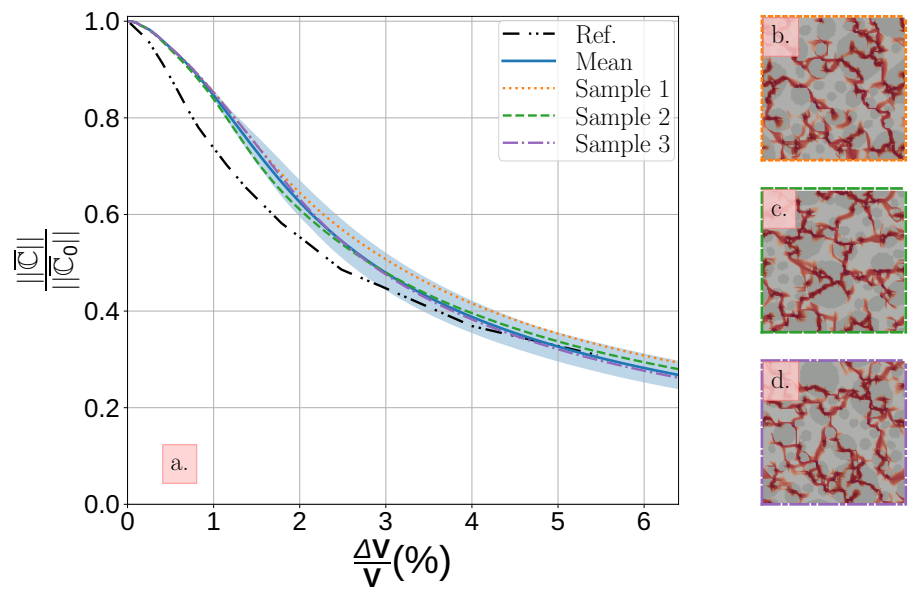


Figure 9: Stiffness reduction of sample micro-structures are shown in subfigure a). The light blue area is the area shaped between the maximum and minimum stiffness reduction of 100 samples. The solid blue line is the mean value of the stiffness reduction and the other 3 lines are the results corresponding to three representative micro-structures. Subfigures b. to d. show the final crack pattern developed in the micro-structure corresponding to the three samples (sample 1, 2 , and 3) noted in the subfigure a.

and trust-region solvers in problems without easy access to the explicit objective function, for instance non-linear mechanical homogenization problems. As an example, we show, in this paper, how the introduced incremental energy functional makes the use of trust-region Newton-CG for computational homogenization possible.

We used the modified trust region solver to solve a minimal 1D non-convex problem where the obtained solution was shown to be in agreement with that of standard trust region Newton-CG solvers. Next, we used it to solve a convex homogenization problem; finally, we simulated and studied a real-world homogenization problem with non-convex energy functional, namely meso-scale ASR damage, was simulated and studied by means of the presented modified trust region solver. The obtained results were compared to those reported in the literature [6] with much lower computational cost which made our solution roughly 200 times faster.

Algorithm 1 Pseudo-algorithm of CG-Steihaug solver with reset

```

1: Solve for  $\mathbf{r}$  with system Matrix  $\mathbb{B}$  and initial RHS  $\mathbf{b}_0$ 
2:  $\eta_{CG}$  ▷ CG tol.
3:  $j_{CG,max}$  ▷ max iterations of CG
4: Set  $\mathbf{r}_0 \leftarrow \mathbf{0}, \mathbf{b}_0 \leftarrow \mathbf{b}, \mathbf{d}_0 \leftarrow -\mathbf{b}_0$  ▷ initialization

5: if  $\|\mathbf{b}\| \leq \eta_{cg}$  then
6:   Return  $\mathbf{p}_i = \mathbf{r}_0 = \mathbf{0}$  ▷ already at solution

7: for  $j = 0, 1, 2, \dots, j_{CG,max}$  do
8:   if  $\mathbf{d}_j^T \mathbb{B}_i \mathbf{d}_j \leq 0$  then ▷ non-convex
9:     find  $\tau$  such that  $\mathbf{p}_i = \mathbf{r}_j + \tau \mathbf{d}_j$  minimizes  $m_i(p_i)$ 
       and satisfies  $\|\mathbf{p}_i\| = R_i$ 
10:    Return  $\mathbf{p}_i$ 

11:    $\alpha_j \leftarrow \mathbf{r}_j^T \mathbf{r}_j / \mathbf{d}_j^T \mathbb{B}_i \mathbf{d}_j$ 
12:    $\mathbf{r}_{j+1} \leftarrow \mathbf{r}_j + \alpha_j \mathbf{d}_j$  ▷ update the iterate

13:   if  $\|\mathbf{r}_{j+1}\| \geq R_i$  then ▷ hit the boundary of trust region
14:     find  $\tau$  such that  $\mathbf{p}_i = \mathbf{r}_j + \tau \mathbf{d}_j$  minimizes  $m_i(p_i)$ 
       and satisfies  $\|\mathbf{p}_i\| = R_i$ 
15:     Return  $\mathbf{p}_i$ 

16:   if  $\|\mathbf{r}_{j+1}\| \leq \eta_{cg}$  then ▷ convergence satisfied
17:     Return  $\mathbf{p}_i = \mathbf{r}_{j+1}$ 

18:   if  $\mathbf{r}_{j+1} \cdot \mathbf{r}_j / \mathbf{r}_{j+1} \cdot \mathbf{r}_{j+1} > 0.2$  then ▷ successive steps are not conjugate
19:      $\mathbf{r}_{j+1} = \mathbb{B} \mathbf{r}_j - \mathbf{b}_j$  ▷ reset CG
20:      $\beta_{j+1} \leftarrow 0$  ▷ reset CG
21:   else
22:      $\beta_{j+1} \leftarrow \mathbf{r}_{j+1}^T \cdot \mathbf{r}_{j+1} / \mathbf{r}_j^T \cdot \mathbf{r}_j$ 

23:    $\mathbf{d}_{j+1} \leftarrow -\mathbf{r}_{j+1} + \beta_{j+1} \mathbf{d}_j$  ▷ compute new update direction

```

Algorithm 2 Pseudo-algorithm of projection-based Newton-CG trust-region algorithm in small strain formulation

```

1: Initialize:
2:  $\eta_{\text{eq}}, \eta_{\text{NR}}, \eta_{\text{CG}}, \eta_{\text{up}}$            $\triangleright$  equilibrium-, Newton, CG and update tol.
3:  $i_{\text{NR,max}}, i_{\text{CG,max}}$                  $\triangleright$  max iterations Newton-Raphson and CG
4:  $R, R_{\text{max}}$                            $\triangleright$  trust region radius, maximum radius
5:  $\boldsymbol{\varepsilon} = \mathbf{0}$                  $\triangleright$  small-strain initial guess

6: for  $\Delta\boldsymbol{\varepsilon} = \Delta\boldsymbol{\varepsilon}_1, \Delta\boldsymbol{\varepsilon}_2, \dots$  do           $\triangleright$  macroscopic strain increments
7:    $\boldsymbol{\varepsilon} = \boldsymbol{\varepsilon} + \Delta\boldsymbol{\varepsilon}$            $\triangleright$  increment grad with load step
8:    $\boldsymbol{\varepsilon}_{\text{eval}} = \boldsymbol{\varepsilon} + \boldsymbol{\varepsilon}_{\text{eig}}$            $\triangleright$  adding eigenstrain if needed
9:    $\boldsymbol{\sigma}, \mathbb{B} = \boldsymbol{\sigma}(\boldsymbol{\varepsilon}_{\text{eval}}), \mathbb{B}(\boldsymbol{\varepsilon}_{\text{eval}})$            $\triangleright$  evaluate stress and tangent
10:   $\mathbf{b} = -\mathbb{G} : \boldsymbol{\sigma}(\boldsymbol{\varepsilon}_{\text{eval}})$            $\triangleright$  RHS calculation
11:  if  $\|\mathbf{b}\| \leq \eta_{\text{eq}}$  then
12:    Newton-Raphson converged
13:    Go to line 6           $\triangleright$  linear problem, next load step
14:  for  $i = 0, 1, 2, \dots, i_{\text{NR,max}}$  do           $\triangleright$  Newton-Raphson iteration
15:    Prepare coefficient matrix of the linearized equation  $\mathbb{G} : \mathbb{B} : \delta\boldsymbol{\varepsilon} = \mathbf{b}$ 
16:    Solve  $\mathbb{G} : \mathbb{B} : \delta\boldsymbol{\varepsilon} = \mathbf{b}$  for  $\delta\boldsymbol{\varepsilon}$  with Steihaug CG [55]:
17:      in  $i_{\text{CG,max}}$  steps to accuracy  $\eta_{\text{CG}}$ , Algorithm 1
18:       $\Delta m_i = \boldsymbol{\sigma} : \delta\boldsymbol{\varepsilon} + 1/2 \delta\boldsymbol{\varepsilon} : \mathbb{B} : \delta\boldsymbol{\varepsilon}$            $\triangleright$  energy model change
19:       $\boldsymbol{\sigma}^{\text{trial}} = \boldsymbol{\sigma}(\boldsymbol{\varepsilon} + \delta\boldsymbol{\varepsilon})$            $\triangleright$  stress evaluation with trial strain
20:       $\overline{\Delta W} = 1/2 (\boldsymbol{\sigma} : \delta\boldsymbol{\varepsilon} + \boldsymbol{\sigma}^{\text{trial}} : \delta\boldsymbol{\varepsilon})$            $\triangleright$  1st order energy approx. change
21:       $\bar{\rho} = \overline{\Delta W} / \Delta m_i$ 
22:      if  $\bar{\rho} < 1/4$  then
23:         $R \leftarrow 1/4 R$            $\triangleright$  shrink trust region
24:      else
25:        if  $\bar{\rho} > 3/4$  and  $\|\delta\boldsymbol{\varepsilon}\| = R$  then
26:           $R \leftarrow \min(2R, R_{\text{max}})$            $\triangleright$  expand trust region if possible
27:        if  $\bar{\rho} > \eta_{\text{up}}$  then
28:           $\boldsymbol{\varepsilon} \leftarrow \boldsymbol{\varepsilon} + \delta\boldsymbol{\varepsilon}$            $\triangleright$  increment grad with accepted solution step
29:           $r_{\text{NR}} = \|\delta\boldsymbol{\varepsilon}\| / \|\boldsymbol{\varepsilon}\|$            $\triangleright$  calculating relative residual
30:           $\boldsymbol{\varepsilon}_{\text{eval}} = \boldsymbol{\varepsilon} + \boldsymbol{\varepsilon}_{\text{eig}}$            $\triangleright$  adding eigen strain if needed
31:           $\boldsymbol{\sigma}, \mathbb{B} = \boldsymbol{\sigma}(\boldsymbol{\varepsilon}_{\text{eval}}), \mathbb{B}(\boldsymbol{\varepsilon}_{\text{eval}})$            $\triangleright$  evaluate stress and tangent
32:           $\mathbf{b} = -\mathbb{G} : \boldsymbol{\sigma}(\boldsymbol{\varepsilon}_{\text{eval}})$            $\triangleright$  RHS calculation with updated grad
33:          if  $\|\delta\boldsymbol{\varepsilon}\| < R$  then
34:            if  $\|\mathbf{b}\| \leq \eta_{\text{eq}}$  or  $r_{\text{NR}} \leq \eta_{\text{NR}}$  then
35:              Newton-Raphson is converged
36:              Go to line 6           $\triangleright$  next load step
37:            else
38:              Go to line 14           $\triangleright$  next Newton loop iteration
39:          else
40:            Go to line 14           $\triangleright$  next Newton loop iteration
41:        else
42:          Trial step rejected
43:          Go to line 14           $\triangleright$  next Newton loop iteration

```

Acknowledgments

We acknowledge funding by the the Swiss National Science Foundation (Ambizione grant 174105 (TJ)), European Research Council (StG-757343 (LP)), the Carl Zeiss Foundation (Research cluster "Interactive and Programmable Materials - IPROM" (LP)), the Deutsche Forschungsgemeinschaft (EXC 2193/1 - 390951807 (LP)), the Czech Science Foundation (projects No. 20-14736S (ML) and 19-26143X (JZ)), and the European Regional Development Fund (Centre of Advanced Applied Sciences – CAAS, CZ.02.1.01/0.0/0.0/16_019/0000778 (ML, IP)). We also would like to acknowledge Prof. Jan Zeman, Prof. Lars Patweska and Prof. Ivana Pultarová for their help and guidance in writing the paper.

Appendix A. Damage material

The scalar damage measure D used in (22) is a function of the highest control variable κ that the material had experienced in the solution history. Different definitions of the control variable κ result in different damage models. Here, for instance, both phases are assumed to be only damaging in tension. To this end the damage control measure is considered as:

$$\kappa = \left\| \boldsymbol{\varepsilon}^{(t)} \right\|, \text{ with } \boldsymbol{\varepsilon}^{(t)} = \mathcal{H}(\epsilon_i) \mathbf{q}_i, \quad (\text{A.1})$$

where \mathcal{H} is the Heaviside function, ϵ_i is the i^{th} eigenvalue of the strain tensor and \mathbf{q}_i is its corresponding eigenvector. This failure criterion suites ASR damage simulation when cracking under tension (Mode-I fracture) is the effective damage mechanism. The damage variable evolves according to the flow rule of

$$\dot{D} = \begin{cases} 0 & \text{if } f < 0 \text{ or } f = 0 \text{ and } \dot{f} < 0, \text{ and } \dot{\phi} < 0, \\ \Phi(\boldsymbol{\varepsilon}, D) & \text{if } f = 0, \text{ and } \dot{f} = 0 \end{cases} \quad (\text{A.2})$$

where $\Phi(\boldsymbol{\varepsilon}, D)$, called the damage evolution function is a positive function of the strain and damage variable. The damage loading surface f corresponds to the damage threshold of the material. In the bilinear scalar damage evolution considered here, the damage variable can be calculated according to:

$$D = \frac{(\kappa - \kappa_0)(1 + \alpha)}{\kappa} \quad (\text{A.3})$$

where κ_0 is the initial strain measure damage threshold and α is the relative slope of the softening part of the constitutive law, depicted in Figure 6a.

It is notable that computing the tangent stiffness of the constitutive law, needed due to using Newton-CG solvers, can introduce singularity because it involves differentiation of κ with respect to $\boldsymbol{\varepsilon}$. According to (A.1) this differentiation needs differentiation of strain eigenvectors (\mathbf{q}_i) with respect to the strain tensor itself with the form of:

$$\frac{\partial \mathbf{q}_{i,\gamma}}{\partial \boldsymbol{\varepsilon}_{\alpha\beta}} = \sum_{i \neq j} \frac{\mathbf{q}_{i,\beta} \mathbf{q}_{j,\alpha}}{\epsilon_i - \epsilon_j} \mathbf{q}_{j,\gamma} \quad (\text{A.4})$$

which can cause singularity in case $\epsilon_i - \epsilon_j$ tends to 0. In order to resolve this problem, we have reformulated the $\boldsymbol{\varepsilon}^{(t)}$ by defining a so called masking matrix $\mathbf{M}^{(t)}$ based on the spectral decomposition of $\boldsymbol{\varepsilon}$ (inspired by [5]) according to:

$$\boldsymbol{\varepsilon}^{(t)} = \mathbf{M}^{(t)} \boldsymbol{\varepsilon} \mathbf{M}^{(t)} \quad (\text{A.5})$$

where $\mathbf{M}^{(t)}$ is defined as:

$$\mathbf{M}^{(t)} = \sum_{i=1}^d \mathcal{H}(\epsilon_i) \mathbf{q}_i \otimes \mathbf{q}_i. \quad (\text{A.6})$$

Working out the differentiation of $\boldsymbol{\varepsilon}^{(t)}$ expression with respect to $\boldsymbol{\varepsilon}$ according to (A.5) and (A.6) singularity is avoided in the explicit stiffness tangent formulation.

References

- [1] Z. P. Bažant. Instability, ductility, and size effect in strain-softening concrete. *Journal of the Engineering Mechanics Division*, 102(2):331–344, apr 1976. doi: 10.1061/jmcea3.0002111.
- [2] B. Budiansky. On the elastic moduli of some heterogeneous materials. *J. Mech. Phys. Solids*, 13(4):223–227, 1965.
- [3] R. H. Byrd, J. C. Gilbert, and J. Nocedal. A trust region method based on interior point techniques for nonlinear programming. *Math. Program.*, 89(1):149–185, 2000.
- [4] A. R. Conn, N. I. Gould, and P. L. Toint. *Trust region methods*. SIAM, 2000.
- [5] L. Contrafatto and M. Cuomo. Comparison of two forms of strain decomposition in an elastic-plastic damaging model for concrete. *Modelling and Simulation in Materials Science and Engineering*, 15(4):S405–S423, May 2007. ISSN 1361-651X. URL <http://dx.doi.org/10.1088/0965-0393/15/4/S07>.
- [6] A. I. Cuba Ramos. *Multi-Scale Modeling of the Alkali-Silica Reaction in Concrete*. PhD thesis, EPFL, Lausanne, 2017. URL <http://infoscience.epfl.ch/record/227479>.
- [7] A. I. Cuba Ramos, C. Roux-Langlois, C. F. Dunant, M. Corrado, and J.-F. Molinari. HPC simulations of alkali-silica reaction-induced damage: Influence of alkali-silica gel properties. *Cement Concrete Res.*, 109:90–102, 2018. ISSN 0008-8846. doi: 10.1016/j.cemconres.2018.03.020.
- [8] F. E. Curtis and X. Que. A quasi-Newton algorithm for nonconvex, nonsmooth optimization with global convergence guarantees. *Mathematical Programming Computation*, 7(4):399–428, Dec. 2015. ISSN 1867-2957. URL <https://doi.org/10.1007/s12532-015-0086-2>.

- [9] Y.-H. Dai, L.-Z. Liao, and D. Li. On restart procedures for the conjugate gradient method. *Numerical Algorithms*, 35(2):249–260, 2004.
- [10] T. W. J. de Geus, J. Vondřejc, J. Zeman, R. H. J. Peerlings, and M. Geers. Finite strain FFT-based non-linear solvers made simple. *Comput. Method. Appl. M.*, 318:412–430, 2017. ISSN 0045-7825. doi: 10.1016/j.cma.2016.12.032.
- [11] M. J. DeJong, M. A. Hendriks, and J. G. Rots. Sequentially linear analysis of fracture under non-proportional loading. *Eng. Fract. Mech.*, 75(18): 5042–5056, 2008.
- [12] P. Eisenlohr, M. Diehl, R. Lebensohn, and F. Roters. A spectral method solution to crystal elasto-viscoplasticity at finite strains. *Int. J. Plast.*, 46:37 – 53, 2013. ISSN 0749-6419. doi: <https://doi.org/10.1016/j.ijplas.2012.09.012>. URL <http://www.sciencedirect.com/science/article/pii/S0749641912001428>. Microstructure-based Models of Plastic Deformation.
- [13] J. D. Eshelby. The determination of the elastic field of an ellipsoidal inclusion, and related problems. *P. Roy. Soc. A-Math. Phys.*, 241(1226): 376–396, 1957. doi: 10.1098/rspa.1957.0133.
- [14] J. D. Eshelby. The elastic field outside an ellipsoidal inclusion. *P. Roy. Soc. A-Math. Phys.*, 252(1271):561–569, 1959. doi: 10.1098/rspa.1959.0173.
- [15] M. Frigo and S. G. Johnson. The design and implementation of FFTW3. *Proc. IEEE*, 93(2):216–231, 2005.
- [16] E. R. Gallyamov, A. C. Ramos, M. Corrado, R. Rezakhani, and J.-F. Molinari. Multi-scale modelling of concrete structures affected by alkali-silica reaction: Coupling the mesoscopic damage evolution and the macroscopic concrete deterioration. *Int. J. Solids Struct.*, 207:262–278, 2020.
- [17] M. G. D. Geers, V. G. Kouznetsova, and W. A. M. Brekelmans. Multi-scale computational homogenization: Trends and challenges. *J. Comput. Appl. Math.*, 234(7):2175–2182, 2010. ISSN 0377-0427. doi: 10.1016/j.cam.2009.08.077.
- [18] A. Gelb and S. Gottlieb. The resolution of the Gibbs phenomenon for Fourier spectral methods. *Advances in The Gibbs Phenomenon. Sampling Publishing, Potsdam, New York*, 2007.
- [19] L. Gélébart and R. Mondon-Cancel. Non-linear extension of FFT-based methods accelerated by conjugate gradients to evaluate the mechanical behavior of composite materials. *Computational Materials Science*, 77:430–439, 2013.

- [20] D. Gottlieb and C.-W. Shu. On the Gibbs phenomenon III: recovering exponential accuracy in a sub-interval from a spectral partial sum of a piecewise analytic function. *SIAM J. Numer. Anal.*, 33(1):280–290, 1996.
- [21] D. Gottlieb and C.-W. Shu. On the Gibbs phenomenon and its resolution. *SIAM Rev.*, 39(4):644–668, 1997. doi: 10.1137/S0036144596301390.
- [22] E. Hewitt and R. E. Hewitt. The Gibbs-Wilbraham phenomenon: An episode in Fourier analysis. *Arch. Hist. Exact Sci.*, pages 129–160, 1979.
- [23] R. Hill. Elastic properties of reinforced solids: some theoretical principles. *J. Mech. Phys. Solids*, 11(5):357–372, 1963.
- [24] R. Hill. On the micro-to-macro transition in constitutive analyses of elastoplastic response at finite strain. In *Mathematical proceedings of the Cambridge philosophical society*, volume 98, pages 579–590. Cambridge University Press, Cambridge University Press (CUP), nov 1985. doi: 10.1017/S0305004100063787.
- [25] D. W. Hobbs. *Alkali-silica reaction in concrete*. Thomas Telford Publishing, 1988.
- [26] C.-Y. Hsia, Y. Zhu, and C.-J. Lin. A study on trust region update rules in Newton methods for large-scale linear classification. In *Asian conference on machine learning*, pages 33–48. PMLR, 2017.
- [27] T. Junge. <https://gitlab.com/muspectre/muspectre>, 2022.
- [28] M. Kabel, T. Böhlke, and M. Schneider. Efficient fixed point and Newton-krylov solvers for FFT-based homogenization of elasticity at large deformations. *Comput. Mech.*, 54(6):1497–1514, Dec. 2014. ISSN 1432-0924. URL <https://doi.org/10.1007/s00466-014-1071-8>.
- [29] M. Kabel, D. Merkert, and M. Schneider. Use of composite voxels in FFT-based homogenization. *Computer Methods in Applied Mechanics and Engineering*, 294:168–188, 2015.
- [30] M. Khorrami, J. R. Mianroodi, P. Shanthraj, and B. Svendsen. Development and comparison of spectral algorithms for numerical modeling of the quasi-static mechanical behavior of inhomogeneous materials. *arXiv:2009.03762*, 2020.
- [31] J. Kochmann, L. Ehle, S. Wulfinghoff, J. Mayer, B. Svendsen, and S. Reese. Efficient multiscale FE-FFT-based modeling and simulation of macroscopic deformation processes with non-linear heterogeneous microstructures. In *Multiscale Modeling of Heterogeneous Structures*, pages 129–146. Springer, 2018.

- [32] M. Ladecký, I. Pultarová, and J. Zeman. Guaranteed two-sided bounds on all eigenvalues of preconditioned diffusion and elasticity problems solved by the finite element method. *Appl. Math.*, 66(1):21–42, jan 2021. doi: 10.21136/AM.2020.0217-19.
- [33] M. Ladecký, R. J. Leute, A. Falsafi, I. Pultarová, L. Pastewka, T. Junge, and J. Zeman. Optimal FFT-accelerated finite element solver for homogenization, 2022. URL <https://arxiv.org/abs/2203.02962>.
- [34] M. Leuschner and F. Fritzen. Fourier-accelerated nodal solvers (fans) for homogenization problems. *Comput. Mech.*, 62(3):359–392, Sep 2018. ISSN 1432-0924. doi: 10.1007/s00466-017-1501-5. URL 10.1007/s00466-017-1501-5.
- [35] R. J. Leute, M. Ladecký, A. Falsafi, I. Jödicke, I. Pultarová, J. Zeman, T. Junge, and L. Pastewka. Elimination of ringing artifacts by finite-element projection in FFT-based homogenization. *J. Comput. Phys.*, page 110931, 2022.
- [36] A. Li. *”Micro-architected Metamaterials: Design and Analysis”*. Mechanical engineering research theses and dissertations. 2., Southern Methodist University, 2017. URL https://scholar.smu.edu/engineering_mechanical_etds/2.
- [37] C. Liu, P. Sharma, P. Newell, J. E. Bishop, A. Spear, B. T. Lester, G. M. Castelluccio, M. Bonney, and M. R. Brake. Emergent homogenization techniques and effective dynamical properties. Technical report, Sandia National Lab.(SNL-NM), Albuquerque, NM (United States), 2016.
- [38] S. Lucarini and J. Segurado. An algorithm for stress and mixed control in galerkin-based FFT homogenization. *Int. J. Numer. Methods Eng.*, 119(8): 797–805, 2019.
- [39] X. Ma, M. Shakoor, D. Vasiukov, S. V. Lomov, and C. H. Park. Numerical artifacts of fast Fourier transform solvers for elastic problems of multi-phase materials: their causes and reduction methods. *Comput. Mech.*, pages in press, , 2021. doi: 10.1007/s00466-021-02013-5.
- [40] X. Ma, M. Shakoor, D. Vasiukov, S. V. Lomov, and C. H. Park. Numerical artifacts of fast Fourier transform solvers for elastic problems of multi-phase materials: their causes and reduction methods. *Comput. Mech.*, 67(6):1661–1683, 2021.
- [41] M. Marvi-Mashhadi, C. Lopes, and J. LLorca. High fidelity simulation of the mechanical behavior of closed-cell polyurethane foams. *J. Mech. Phys. Solids*, 135:103814, 2020. ISSN 0022-5096. doi: <https://doi.org/10.1016/j.jmps.2019.103814>. URL <https://www.sciencedirect.com/science/article/pii/S0022509619306477>.

- [42] K. Matouš, M. G. Geers, V. G. Kouznetsova, and A. Gillman. A review of predictive nonlinear theories for multiscale modeling of heterogeneous materials. *J. Comput. Phys.*, 330:192–220, feb 2017. ISSN 10902716. doi: 10.1016/j.jcp.2016.10.070.
- [43] J. Mazars and G. Pijaudier-Cabot. Continuum damage theory—application to concrete. *J. Eng. Mech.*, 115(2):345–365, 1989.
- [44] C. Meng, W. Heltsley, and D. D. Pollard. Evaluation of the Eshelby solution for the ellipsoidal inclusion and heterogeneity. *Comput. Geosci.*, 40:40–48, 2012. ISSN 0098-3004. doi: 10.1016/j.cageo.2011.07.008.
- [45] J. C. Michel, H. Moulinec, and P. Suquet. A computational scheme for linear and non-linear composites with arbitrary phase contrast. *Int. J. Numer. Methods Eng.*, 52(1-2):139–160, 2001. doi: 10.1002/nme.275. URL <https://onlinelibrary.wiley.com/doi/abs/10.1002/nme.275>.
- [46] G. W. Milton. The theory of composites. *Materials and Technology*, 117: 483–93, 1995.
- [47] G. W. Milton and A. Sawicki. Theory of composites. cambridge monographs on applied and computational mathematics. *Appl. Mech. Rev.*, 56 (2):B27–B28, 2003.
- [48] N. Mishra, J. Vondřejc, and J. Zeman. A comparative study on low-memory iterative solvers for FFT-based homogenization of periodic media. *J. Comput. Phys.*, 321:151–168, 2016. ISSN 0021-9991. doi: <https://doi.org/10.1016/j.jcp.2016.05.041>. URL <https://www.sciencedirect.com/science/article/pii/S0021999116301863>.
- [49] T. Mori and K. Tanaka. Average stress in matrix and average elastic energy of materials with misfitting inclusions. *Acta Metall.*, 21(5):571–574, 1973.
- [50] J. Moshfegh and M. N. Vouvakis. Direct solution of FEM models: Are sparse direct solvers the best strategy?, 2020.
- [51] S. MotahariTabari and I. Shooshpasha. Evaluation of coarse-grained mechanical properties using small direct shear test. *Int. J. Geotech. Eng.*, 15 (6):667–679, aug 2018. doi: 10.1080/19386362.2018.1505310.
- [52] H. Moulinec and P. Suquet. A fast numerical method for computing the linear and nonlinear properties of composites. *C. R. Acad. Sci. II B-Mec.*, 318:1417–1423, 01 1994.
- [53] T. Mura. *Micromechanics of Defects in Solids*. Kluwer Academic Publishers Group, 1982. ISBN 978-94-011-8548-6. doi: 10.1007/978-94-011-9306-1.
- [54] S. Nemat-Nasser and M. Hori. *Micromechanics: overall properties of heterogeneous materials*. Elsevier, 2013.

- [55] J. Nocedal and S. Wright. *Numerical optimization*. Springer Science & Business Media, 2006.
- [56] A. Norris. A differential scheme for the effective moduli of composites. *Mech. Mater.*, 4(1):1–16, 1985.
- [57] M. Pari, J. G. Rots, and M. Hendriks. Recent advancements in sequentially linear analysis (SLA) type solution procedures. In *Computational Modelling of Concrete and Concrete Structures*, pages 432–442. CRC Press, 2022.
- [58] G. Pijaudier-Cabot and Z. P. Bažant. Nonlocal damage theory. *J. Eng. Mech.*, 113(10):1512–1533, 1987.
- [59] M. Pippig. PFFT: An extension of FFTW to massively parallel architectures. *SIAM Journal on Scientific Computing*, 35(3):C213–C236, jan 2013. doi: <https://doi.org/10.1137/120885887>.
- [60] D. Pivovarov, P. Steinmann, and K. Willner. Two reduction methods for stochastic FEM based homogenization using global basis functions. *Computer Methods in Applied Mechanics and Engineering*, 332:488–519, 2018.
- [61] M. J. D. Powell. Restart procedures for the conjugate gradient method. *Math. Program.*, 12(1):241–254, 1977.
- [62] A. Prakash and R. Lebensohn. Simulation of micromechanical behavior of polycrystals: finite elements versus fast Fourier transforms. *Modell. Simul. Mater. Sci. Eng.*, 17(6):064010, 2009.
- [63] I. Pultarová and M. Ladecký. Two-sided guaranteed bounds to individual eigenvalues of preconditioned finite element and finite difference problems. *Numerical Linear Algebra with Applications*, 28(5):e2382, 2021.
- [64] F. Roters, M. Diehl, P. Shanthraj, R. Lebensohn, and P. Eisenlohr. A spectral method solution to crystal elastoviscoplasticity at finite strains. In *Plasticity’13, The 19th International Symposium on Plasticity & Its Current Applications*, 2013.
- [65] J. Rots. Sequentially linear continuum model for concrete fracture. *Fracture mechanics of concrete structures*, 2:831–840, 2001.
- [66] J. G. Rots. *Computational modeling of concrete fracture*. PhD thesis, Czech University of Life Sciences Prague, 1988.
- [67] J. G. Rots and S. Invernizzi. Regularized sequentially linear saw-tooth softening model. *Int. J. Numer. Anal. Methods Geomech.*, 28(7-8):821–856, 2004.
- [68] J. G. Rots, B. Belletti, and S. Invernizzi. Robust modeling of rc structures with an “event-by-event” strategy. *Eng. Fract. Mech.*, 75(3-4):590–614, 2008.

- [69] M. Schneider. A review of nonlinear FFT-based computational homogenization methods. *Acta Mech.*, pages in press, , 2021. doi: 10.1007/s00707-021-02962-1.
- [70] M. Schneider, F. Ospald, and M. Kabel. Computational homogenization of elasticity on a staggered grid. *Int. J. Numer. Meth. Eng.*, 105(9):693–720, 2016. doi: 10.1002/nme.5008.
- [71] J. Schroder. *A numerical two-scale homogenization scheme: the FE2-method*, pages 1–64. Springer Vienna, Vienna, 2014. ISBN 978-3-7091-1625-8. doi: 10.1007/978-3-7091-1625-8_1. URL https://doi.org/10.1007/978-3-7091-1625-8_1.
- [72] A. Sellier, É. Grimal, S. Multon, and E. Bourdarot. *Swelling concrete in dams and hydraulic structures: DSC 2017*. John Wiley & Sons, 2017.
- [73] T. Steihaug. The conjugate gradient method and trust regions in large scale optimization. *SIAM J. Numer. Anal.*, 20(3):626–637, 1983.
- [74] R. Swamy. *The Alkali-Silica Reaction in Concrete*. CRC Press, 1991.
- [75] V. Vinogradov and G. W. Milton. An accelerated FFT algorithm for thermoelastic and non-linear composites. *Int. J. Numer. Methods Eng.*, 76(11):1678–1695, 2008. doi: 10.1002/nme.2375. URL <https://onlinelibrary.wiley.com/doi/abs/10.1002/nme.2375>.
- [76] J. Vondřejc, J. Zeman, and I. Marek. An FFT-based Galerkin method for homogenization of periodic media. *Comput. Math. Appl.*, 68(3):156–173, 2014. ISSN 0898-1221. doi: 10.1016/j.camwa.2014.05.014.
- [77] D. Wicht, M. Schneider, and T. Böhlke. On quasi-newton methods in fast fourier transform-based micromechanics. *International Journal for Numerical Methods in Engineering*, 121(8):1665–1694, dec 2019. doi: 10.1002/nme.6283.
- [78] F. Willot. Fourier-based schemes for computing the mechanical response of composites with accurate local fields. *C. R. Mécanique*, 343(3):232–245, 2015. ISSN 1631-0721. doi: 10.1016/j.crme.2014.12.005.
- [79] Y.-x. Yuan. A review of trust region algorithms for optimization. In *Iciam*, volume 99, pages 271–282, 2000.
- [80] J. Zeman, J. Vondřejc, J. Novák, and I. Marek. Accelerating a FFT-based solver for numerical homogenization of periodic media by conjugate gradients. *J. Comput. Phys.*, 229(21):8065–8071, 2010.
- [81] J. Zeman, T. W. J. de Geus, J. Vondřejc, R. H. J. Peerlings, and M. G. D. Geers. A finite element perspective on nonlinear FFT-based micromechanical simulations. *Int. J. Numer. Meth. Eng.*, 111(10):903–926, 2017. doi: 10.1002/nme.5481.